Coupled Cu and Mn charge and orbital orders in $YBa_2Cu_3O_7/Nd_{0.65}(Ca_{1-y}Sr_y)_{0.35}MnO_3$ multilayers

E. Perret[1,2], C. Monney[1,3], S. Johnston[4,5], J. Khmaladze[1], F. Lyzwa[1], R. Gaina[1,6], M. Dantz[7], J. Pelliciari[7], C. Piamonteze[7], B.P.P. Mallett[1,8], M. Minola[9], B. Keimer[9], T. Schmitt[7] & C. Bernhard[1]

The observation of a charge density wave in the underdoped cuprate high T_c superconductors (Cu-CDW) raised a debate about its relationship with superconductivity. In bulk $YBa_2Cu_3O_{7-\delta}$ the Cu-CDW is incipient and mainly pinned by defects. Nevertheless, a large magnetic field can induce a true long-range Cu-CDW order as it suppresses superconductivity. An enhanced Cu-CDW order was also observed in $YBa_2Cu_3O_7/La_{2/3}Ca_{1/3}MnO_3$ multilayers. Here, we show that the magnitude of the Cu-CDW in $YBa_2Cu_3O_{7-\delta}$ / $Nd_{0.65}(Ca_{1-y}Sr_y)_{0.35}MnO_3$ multilayers can be varied by adjusting the strength of the manganite charge and orbital order via the Sr content (tolerance factor). Furthermore, we resolve the reconstruction of the crystal field levels of the interfacial Cu ions that are also affected by the manganite charge and orbital order. This tuneable interfacial coupling and Cu-CDW in $YBa_2Cu_3O_{7-\delta}$ can be used for studying the relationship between the Cu-CDW and superconductivity and, possibly, for inducing new intertwined quantum states.

[1] Department of Physics and Fribourg Center for Nanomaterials, University of Fribourg, Chemin du Musée 3, 1700 Fribourg, Switzerland. [2] Laboratory for Advanced Fibers, Empa, Swiss Federal Laboratories for Materials Science and Technology, Lerchenfeldstrasse 5, 9014 St. Gallen, Switzerland. [3] Physik-Institut, Universität Zürich, Winterthurerstr 190, 8057 Zürich, Switzerland. [4] Department of Physics and Astronomy, The University of Tennessee, Knoxville, TN 37996, USA. [5] Joint Institute for Advanced Materials, The University of Tennessee, Knoxville, TN 37996, USA. [6] Laboratory for Neutron Scattering and Imaging, Paul Scherrer Institut, 5232 Villigen, Switzerland. [7] Swiss Light Source, Paul Scherrer Institut, 5232 Villigen, Switzerland. [8] The Photon Factory, The University of Auckland, 38 Princes St, Auckland, New Zealand. [9] Max-Planck-Institut für Festkörperforschung, Heisenbergstrasse 1, 70569 Stuttgart, Germany. Correspondence and requests for materials should be addressed to C.M. (email: claude.monney@unifr.ch) or to C.B. (email: christian.bernhard@unifr.ch)

The unusual electronic properties of the cuprate high T_c superconductors are the subject of a controversial discussion since their discovery more than 30 years ago[1]. Of particular interest has been the so-called pseudogap regime in the underdoped part of the doping phase diagram for which the onset of a loss-free superconducting response seems to be controlled by the phase coherence (due to the small condensate density) rather than by the pairing strength. Whereas the role of anti-ferromagnetic correlations and of incommensurate stripe orders were discussed early on, more recently, the observation of a Cu-CDW in underdoped YBa$_2$Cu$_3$O$_{7-\delta}$ (YBCO) is obtaining a lot of attention[2–7]. A central question is whether this Cu-CDW is just competing with superconductivity or whether these two orders have a more complex relationship and can possibly even form so-called intertwined states[8].

The perovskite manganites A$_{1-x}$(Ca$_{1-y}$Sr$_y$)$_x$MnO$_3$ (A = La or a rare earth) are equally well known for the wealth of their electronic and magnetic properties[9,10]. For A = La, an itinerant ferromagnetic ground state prevails in large parts of the phase diagram ($0.2 \leq y \leq 0.45$), where the so-called colossal magnetoresistance (CMR) effect arises from the competition of the double-exchange interaction with Jahn-Teller-type lattice distortions[11]. The former is determined by the kinetic energy or the bandwidth of the charge carriers, which can be modified via the Mn–O bond-angle or the tolerance factor $t = (r_A + r_O)/[\sqrt{2}(r_{Mn} + r_O)]$, where r_A, r_O, and r_{Mn} are the radii of the A-site cation, oxygen and manganese ions, respectively. Upon reducing t the itinerant ferromagnetism gives way to an insulating, antiferromagnetic ground state with a combined charge/orbital order with a wave vector of $Q = (1/4,1/4,0)$ (r.l.u.) for the orbital and $Q = (1/2,0,0)$ or $Q = (0,1/2,0)$ (r.l.u.) for the charge order (in pseudocubic notation)[8,9]. Even though the oxygen ions also seem to be involved in this order[12–15], we denote these electronic orderings in the following (for simplicity) as a manganite charge and orbital order (Mn–COO).

It is well known that the strength of this Mn–COO can be tuned via the Sr:Ca ratio, y, or t, and also by reducing the hole doping, x. For A = Nd and Pr the Mn–COO persists to about $x = 0.3$, albeit with a reduced correlation length and in combination with a canted antiferromagnetic state[9,10]. This variability allows one to make the insulating, antiferromagnetic and Mn–COO state nearly degenerate with the itinerant ferromagnetic state, such that an external magnetic field allows one to suppress the Mn–COO, thereby restoring the itinerant ferromagnetic state[9,10].

Competing orders are also underlying the interface effects in the cuprate/manganite multilayers. Most intensively studied are multilayers from YBCO and the half-metallic La$_{0.67}$(Ca,Sr)$_{0.33}$MnO$_3$ (LCMO or LSMO)[16–23]. Here, the focus has been on the superconducting pair breaking effect due to the interaction with the ferromagnetic manganite[19,21,23] and a magnetic moment that is induced in the interfacial CuO$_2$ layer[17,20,22]. Furthermore, there is evidence for a charge (hole) transfer from YBCO to LCMO and a so-called orbital reconstruction of the interfacial Cu ions, which involves a redistribution of the holes from the Cu 3d$_{x^2-y^2}$ orbitals (where they reside in bulk cuprates) to the Cu 3d$_{3z^2-r^2}$ orbitals[16]. The underlying upward shift of the Cu 3d$_{3z^2-r^2}$ energy level has been explained in terms of the hybridization with the Mn 3d$_{3z^2-r^2}$ level via the straight Cu–O$_{apex}$–Mn bond (CuO$_2$–BaO$_{apex}$–MnO$_2$ layer stacking sequence, with O$_{apex}$ being the apical oxygen of the YBCO) that was observed with transmission electron microscopy (TEM)[24,25]. Evidence for a surprisingly strong coupling between the Mn–COO and superconductivity has been obtained from multi-layers of YBCO and an insulating manganite displaying a Mn–COO order that can be varied with a magnetic field[26]. At low field, where the Mn–COO is strongest, their response is insulator-like and resembles that of a granular superconductor, whereas at high field,

the Mn–COO is suppressed and a coherent superconducting state is restored[26]. These observations call for a study of the relationship between the Mn–COO and the insulator-like, granular super-conducting state and a possibly related Cu-CDW. An induced Cu-CDW has already been observed in YBCO/LCMO multilayers with nominally half-metallic LCMO[27,28].

In the following, we use X-ray linear dichroism (XLD) and resonant inelastic X-ray scattering (RIXS) at the Cu L$_3$-edge to study NCSMO/YBCO/NCSMO (NYN) trilayers and reveal a close relationship between the Cu-CDW in YBCO and the Mn–COO in NCSMO. We also provide evidence that the Mn–COO affects the orbital reconstruction of the interfacial Cu ions and causes a lateral modulation that can act as a template for the Cu-CDW. We investigate two NYN trilayers with different Sr content of $y = 0.2$ and 0.4 and thus different strength of the Mn–COO. As shown in Supplementary Note 1, the zero-field resistance of the $y = 0.2$ trilayer with the stronger Mn–COO exhibits a clear, insulator-like upturn below about 80 K that is not yet fully suppressed at 9 Tesla. For the $y = 0.4$ trilayer, the zero-field resistive upturn is less pronounced and a superconducting transition with an onset temperature of $T_{sc} = 70$ K is restored at 9 Tesla.

Results

Cu charge density wave enhanced by Mn charge orbital order.
Figure 1a shows a sketch of the trilayers and the scattering geometry of the RIXS experiment. Here, the wave vectors of the incident (k_{in}) and scattered (k_{out}) x-rays are fixed and the scattering vector (Q) and its in-plane component ($Q_\parallel$) are varied by rotating the sample with respect to the polar angle δ. The sketch of a RIXS spectrum in Fig. 1b details the spectral signatures involving elastic and inelastic scattering processes that typically occur in the cuprates[29]. First, we focus on the elastic peak (at $\Delta E = 0$ eV energy loss) for which the intensity variation is very sensitive to the scattering signal of the 3d valence electrons from the Cu ions. This setup has provided in the past the first, direct evidence for a Cu-CDW in underdoped YBCO with $Q_\parallel = (1/3,0)$ or $(0,1/3)$ (r.l.u.) (note that the peak is broad along L due to a weak correlation of the Cu-CDW along the c-axis)[2].

Figures 1c, d show measurements of the Cu-CDW at 18 K by monitoring the elastic peak at an incident photon energy $\hbar\omega_{in} = 931.12$ eV, corresponding to the Cu L$_3$-edge absorption resonance of two Nd$_{0.65}$(Ca$_{1-y}$Sr$_y$)$_{0.35}$MnO$_3$(26 nm)/YBa$_2$Cu$_3$O$_7$(7 nm)/ Nd$_{0.65}$(Ca$_{1-y}$Sr$_y$)$_{0.35}$MnO$_3$(13 nm) trilayers with $y = 0.2$ and 0.4, respectively. At $y = 0.2$ we observe a pronounced peak near $Q_\parallel = -0.335(14)$ r.l.u., which we attribute to the well-known Cu-CDW. From its width $\Delta Q_\parallel = 0.014$ (FWHM) we derive a correlation length of about $\xi_a = a(\pi\Delta Q_\parallel)^{-1} = 9.1$ nm with the in-plane lattice parameter $a = 3.87$ Å, which is significantly larger than in underdoped, bulk YBCO[2,30]. We have also measured the dependence of this enhancement of the elastic peak at $Q_\parallel = -0.335$ r.l.u. as a function of the incident photon energy, see Fig. 2a. It displays a pronounced resonance around $\hbar\omega_{in} = 931.2$ eV, which is very close to the maximum of the bulk-sensitive fluorescence yield x-ray absorption spectrum (XAS) ($\hbar\omega_{in} = 931.0$ eV, see below), confirming that the Cu-CDW originates from the CuO$_2$ planes of YBCO and not from the CuO chains[31]. Indeed, the maximum intensity of the Bragg peak for a CDW along the CuO chain would instead occur around 933.8 eV[31]. Further evidence for a well-ordered and static Cu-CDW from within the CuO$_2$ planes is obtained from the temperature dependence of the integrated peak intensity, which reveals a mean-field like transition starting at T_c (Cu-CDW) = 175 K, see Fig. 2b. In comparison, the planar Cu-CDW in underdoped YBCO crystals[1–4] has a more gradual onset and a somewhat lower transition temperature of T_c (Cu-CDW) $\leq$ 150 K[3,4,31]. The Bragg peak due to the ortho-III ordering of the
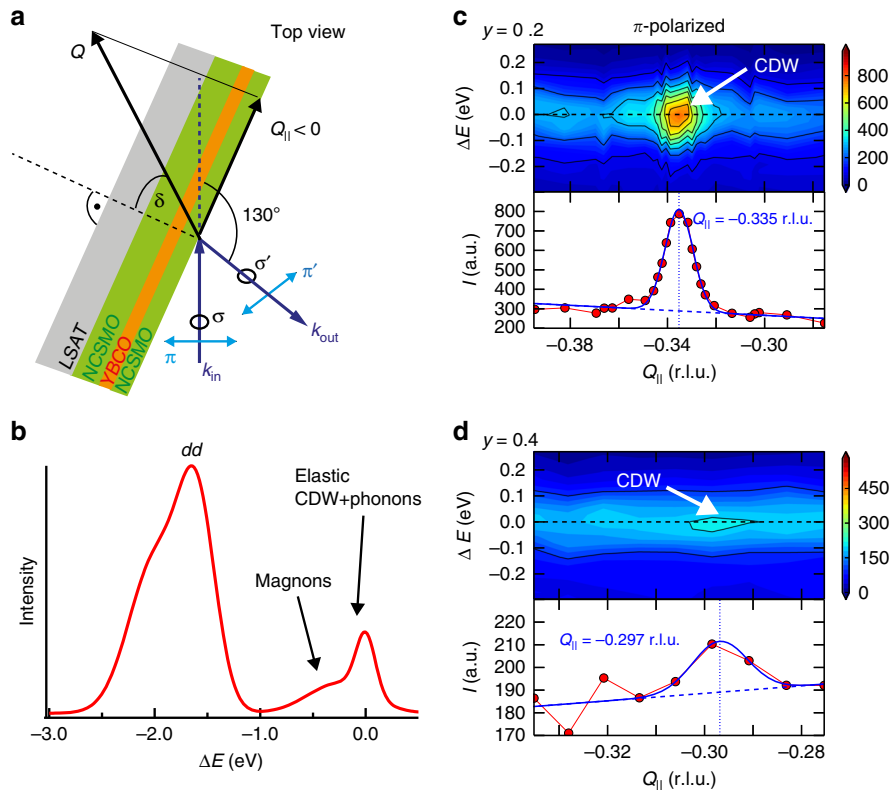
Fig. 1 RIXS study of the copper charge density wave (Cu-CDW) in NCSMO/YBCO/NCSMO trilayers. **a** Scheme of the RIXS experiment. The incident x-ray beam is linearly polarized (π: in-plane, σ: out-of-plane). **b** Schematics of a typical RIXS spectrum of cuprate high-T_c superconductors at the Cu L_3-edge showing the various elastic ($\Delta E = 0$) and inelastic ($\Delta E < 0$) transitions. **c**, **d** Evolution of the elastic peak of the RIXS spectrum versus the in-plane momentum transfer, $Q_\parallel$, measured in π-polarization of the incident light at 18 K and incident photon energy $E_{in} = 931.12$ eV for **c** $y = 0.2$ and **d** 0.4. The upper and lower panels show the RIXS map around the elastic peak and the corresponding line cut at $\Delta E = 0$, respectively
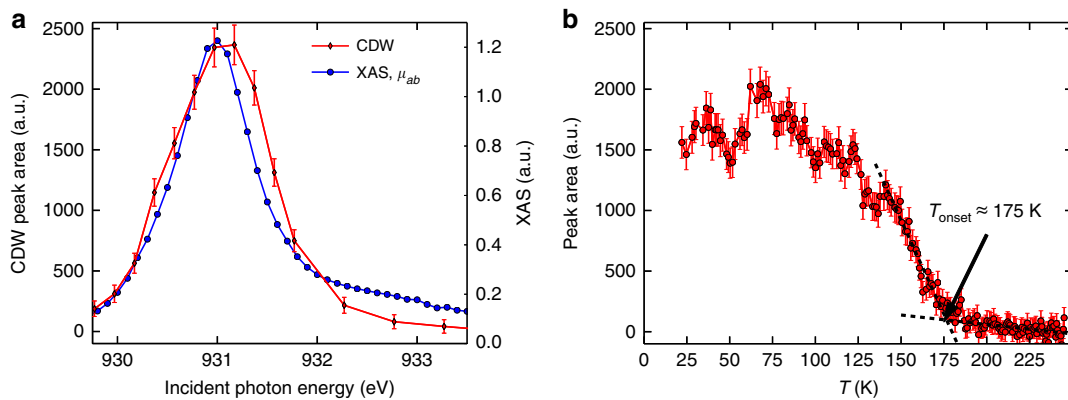

Fig. 2 Incident photon energy and temperature dependence of the copper charge density wave (Cu-CDW). Evolution of the Cu-CDW peak of the $y = 0.2$ trilayer at $Q_\parallel = -0.335$ r.l.u. as a function of **a** the incident photon energy and **b** the temperature. The XAS spectrum measured at the Cu L_3-edge spectra ($T = 5$ K and $H = 0.5$ T) in fluorescence yield (FY) mode is also shown for comparison in **a** for the out-of-plane polarization. In **a** the off-resonant background of 376 counts has been subtracted from the CDW area and in (b) a background of 810 counts due to a temperature independent elastic peak signal has been subtracted. The error bars indicate the s.d. to the number of detected photons

CuO chains, on the other hand, persists well above room temperature [31] and thus can be discarded. For the trilayer with $y = 0.4$ we observe a much weaker Cu-CDW peak that is located at $Q_\parallel = -0.29(3)$ r.l.u. as shown in Fig. 1d. This result constitutes our first major finding: the magnitude of the Cu-CDW in YBCO depends on the strength of the Mn–COO in

NCSMO which at $y = 0.2$ (with $t = 0.952$) is larger than at $y = 0.4$ (with $t = 0.955$).

Strength of the Mn charge and orbital order. The fact that the Mn–COO is weaker for samples with $y = 0.4$ than for samples with $y = 0.2$ can be seen in the magnetoresistance data of the
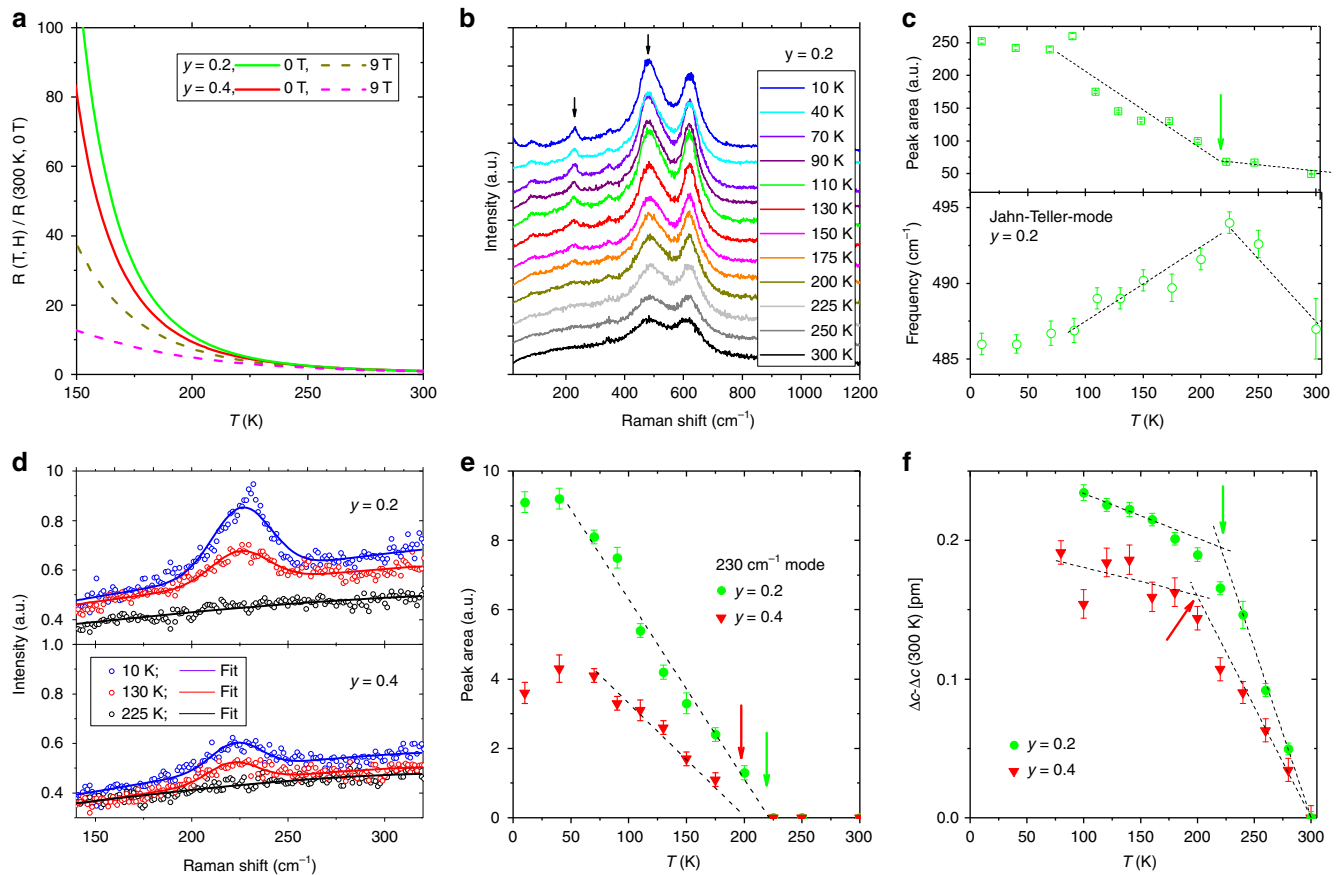
Fig. 3 Signatures of the manganese charge and orbital order (Mn–COO). **a** R-T measurements of NCSMO single layers with $y = 0.2$ and 0.4 in magnetic fields of zero and 9 Tesla (parallel to the layers) which confirm that the effect of the magnetic field is weaker for $y = 0.2$, meaning that the Mn–COO is stronger in this sample. **b** Temperature dependent Raman-spectra of the NYN trilayer with $y = 0.2$ for which vertical offsets are added for clarity. Arrows mark the positions of the "Jahn-Teller-mode" around 480 cm^{-1} and an additional weaker mode around 230 cm^{-1} that appears only in the Mn–COO state. **c** Temperature-dependence of the intensity (upper panel) and the eigenfrequency (lower panel) of the Jahn-Teller-mode obtained by fitting with Gaussian profiles (dotted lines are guides to the eye). **d** Magnified view of the weak mode at 230 cm^{-1} showing its absence at 225 K and Gaussian fits at selected temperatures below T_c (Mn–COO). **e** Temperature dependence of the intensity of the 230 cm^{-1} mode for the NYN trilayers with $y = 0.2$ and 0.4. **f** Evolution of the difference in the c-axis lattice parameters ($\Delta c = c(\text{LSAT})$-$c(\text{NCSMO})$) of the NYN trilayers versus temperature showing a kink at the onset of the Mn–COO around 220 K at $y = 0.2$ and 200 K at $y = 0.4$. The error bars in graphs (**c**), (**e**), and (**f**) reflect the accuracy of the fitting procedure

corresponding NCSMO single layers ($d = 20$ nm). In Fig. 3a the upturn of the resistivity in the Mn–COO state is indeed steeper in zero field and less strongly suppressed by a field of 9 Tesla at $y = 0.2$ than at $y = 0.4$. These curves do not show a pronounced anomaly around the critical temperature of the Mn–COO phase, T_c (Mn–COO), as reported for corresponding single crystals (see e.g., refs. [9,10]). This difference is most likely due to a broadening of the Mn–COO transition that arises from the strain and disorder of such thin films. Figures 3b–d show that the onset of the Mn–COO below T_c (Mn–COO) is also evident from the anomalous temperature dependence of some of the phonon modes in the Raman response of the NYN trilayers. The Raman-active phonon modes of the manganites are known to be very sensitive to the lattice distortions since for the cubic structure they are symmetry forbidden. For single crystals it was shown that the Mn–COO gives rise to an anomalous increase of the intensity of the so-called "Jahn-Teller-mode" around 480 cm^{-1} and of the "breathing mode" around 620 cm^{-1}[32]. This intensity increase was explained in terms of an order-disorder transition from a state with strongly disordered and fluctuating Jahn-Teller distortions above T_c (Mn–COO) to a static and cooperative Jahn-Teller effect

due to the Mn–COO[32]. Figure 3b displays the T-dependent Raman spectra for the $y = 0.2$ trilayer, which exhibit the above described intensity increase of both the Jahn-Teller and the breathing modes in the Mn–COO state. Figure 3c details the evolution of the intensity (upper panel) and eigenfrequency (lower panel) of the "Jahn-Teller mode" that has been obtained by fitting the Raman modes with Gaussian functions. Both parameters exhibit clear anomalies with the onset of the Mn–COO at T_c(Mn–COO) = 220 K. Figure 3d shows a magnified view of an additional, weaker mode around 230 cm^{-1} that is absent above T_c(Mn–COO) = 220 K and develops only in the Mn–COO state. This characteristic behavior was previously also observed in single crystals and explained in terms of a folding of the Brillouin zone due to the enlarged unit cell in the Mn–COO state[32]. Figure 3e confirms that the intensity of this additional mode, which can serve as a measure of the strength of the Mn–COO, is about two times larger at $y = 0.2$ than at $y = 0.4$. Finally, Fig. 3f shows that the onset of the Mn–COO gives rise-to a kink in the T-dependence of the c-axis lattice parameter around T_c (Mn–COO) = 220 K at $y = 0.2$ and T_c (Mn–COO) = 200 K at $y = 0.4$. Combined, these results establish the presence
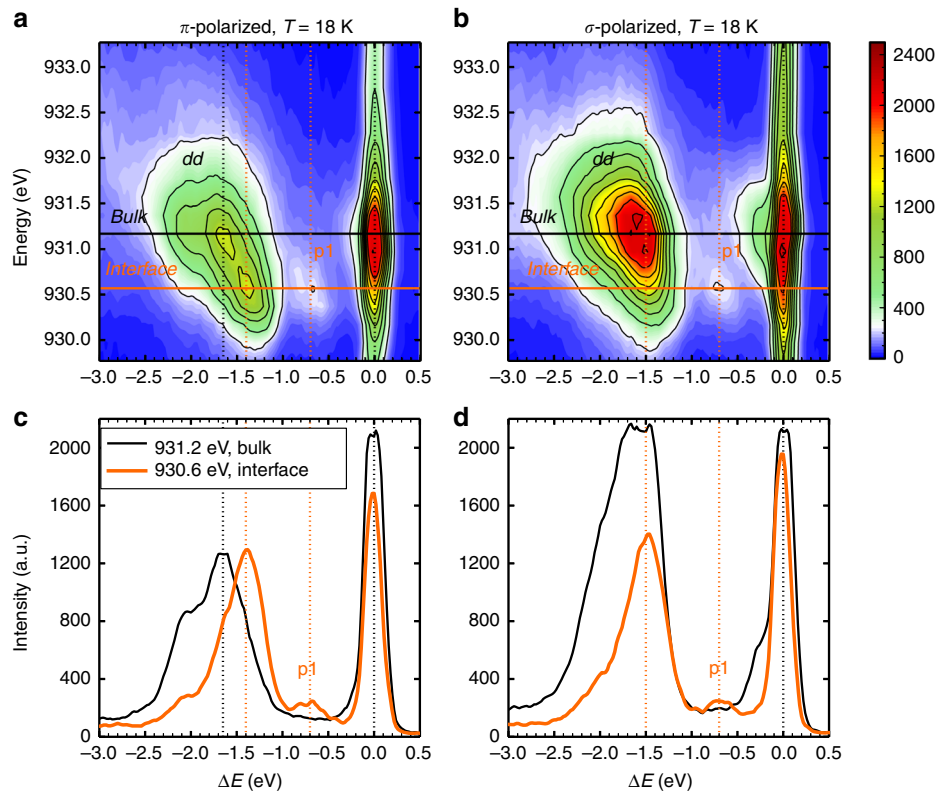
Fig. 4 RIXS spectra showing distinct *dd*-excitations for the interfacial and bulk-like Cu ions. RIXS spectra at 18 K measured **a** in π-polarization and **b** σ-polarization of the incident light at $Q_∥ = -0.33$ r.l.u. for incident energies between 929.8 and 933.3 eV. **c**, **d** Corresponding RIXS spectra at 931.2 and 930.6 eV that are representative of the response of the bulk-like and the interfacial Cu ions, respectively. Note that the p1 peak at $ΔE = -0.7$ eV is only observed for incident x-ray energies close to 930.6 eV

of Mn–COO in our samples, which is strongest in the $y = 0.2$ trilayer.

Cu orbital reconstruction at the interface. Next, we show that the inelastic part of the RIXS spectra contains important information about the reconstruction of the crystal field of the interfacial Cu ions and its interplay with the Mn–COO. Figures 4a, b display maps of the RIXS spectra for π-polarized and σ-polarized incident light respectively as a function of the incident photon energy along the Cu L_3-edge (at 18 K and $Q_∥ = -0.335$ r.l.u.) for the $y = 0.2$ sample, for which a strong Mn–COO order is present in the manganite layer. Single spectra at the selected energies of 930.6 and 931.2 eV are displayed in Figs. 4c, d for the π-polarization and σ-polarization, respectively. The main features, besides the elastic line at $ΔE = 0$ eV, are the *dd*-excitations that exhibit a pronounced dependence on the incident energy. There are two distinct maxima at $ΔE = -1.6$ eV for an incident energy around $ℏω_{in} = 931.2$ eV and at $ΔE = -1.40$ eV for an incident energy $ℏω_{in} = 930.6$ eV, which are marked by the black and orange lines, respectively. In addition, there is a weak peak around $ΔE = -0.7$ eV (labeled p1), which we associate with a *dd*-excitation since it is nondispersive (see the Supplementary Note 2). This distinct p1 peak occurs only for incident photon energies close to 930.6 eV and, to the best of our knowledge, is reported here for the first time in such cuprate/manganite multilayers. Figure 5 compares RIXS spectra measured at an incident photon energy of 930.6 eV with π-polarized light for $y = 0.2$, $y = 0.4$ NYN samples and a YBCO/LCMO superlattice. This comparison shows that the p1 peak at -0.7 eV is more pronounced at $y = 0.2$ than at $y = 0.4$

and is hardly discernible in a YBCO/LCMO superlattice, for which the manganite layers do not have an intrinsic Mn–COO.

The characteristic changes of the RIXS spectra with the incident photon energy can be understood from previous Cu L_3-edge XLD studies of YBCO/LCMO multilayers, which have shown that the maximum of the resonance of the Cu ions next to the interface (interfacial Cu ions) is redshifted by about 0.5 eV with respect to the one of the Cu ions that are further away from the interface (bulk-like Cu ions)[16,33]. Figure 6 shows the corresponding XLD spectra of the NYN trilayers with $y = 0.2$ and $y = 0.4$ and the YBCO/LCMO superlattice (Y/L SL). For all three samples they confirm that the peak of the total electron yield (TEY), which is most sensitive to the uppermost YBCO/manganite interface, is redshifted by about 0.5 eV with respect to the peak of the fluorescence yield (FY), which probes all Cu ions. Accordingly, we argue that the RIXS spectra at 930.6 and 931.2 eV in Fig. 4 are representative of the *dd*-excitations of the interfacial and the bulk-like Cu ions, respectively.

We now discuss the attribution of the different peaks in the RIXS spectra to specific inter-*d*-orbital excitations, called *dd*-excitations. Their energy loss distribution reflects overlapping contributions from the 3*d*-orbitals[34]. In a recent work, the authors of ref. [35] analyzed in detail the Cu L_3-edge RIXS spectra of bulk YBCO and attributed the main peak at around -1.6 eV energy loss to a combined $d_{x^2-y^2} → d_{xy}$ and $d_{x^2-y^2} → d_{xz}/d_{yz}$ excitation of the $3d^9$ hole, while a pronounced shoulder at -2 eV energy loss was attributed to the $d_{x^2-y^2} → d_{3z^2-r^2}$ excitation. This assignment also describes well the RIXS spectra of the bulk-like Cu ions (at $ℏω_{in} = 931.2$ eV) of the $y = 0.2$ NYN sample studied here (see Figs. 4c, d, black curves). In comparison the peaks due
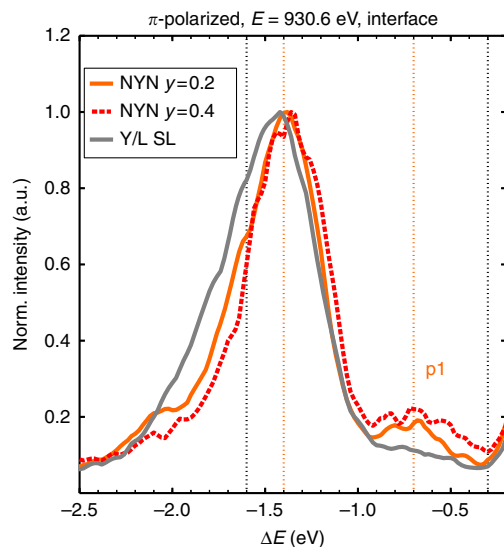
Fig. 5 RIXS spectra showing the effect of the Mn–COO on the *dd* excitations of the interfacial Cu ions. Comparison of the RIXS spectra at 18 K with π-polarization and an energy of 930.6 eV of the incident light that are representative of the response of the interfacial Cu ions for the two trilayers with $y = 0.2$ and $y = 0.4$ and a YBCO/LCMO superlattice without an intrinsic Mn–COO. It shows that the p1 peak, due to the transition from d_{x2-y^2} to $d_{3z^2-r^2}$, is most pronounced for the $y = 0.2$ trilayer with the strongest Mn–COO

to the *dd*-excitations of the interfacial Cu ions are narrower and shifted to smaller energy losses (see Figs. 4c, d, orange curves). This implies that the Cu crystal field is changing from a tetragonal symmetry toward a cubic symmetry, when going from the bulk to the interface. The new p1 peak at $\Delta E = -0.7$ eV, which occurs only at the interface resonance, is interpreted as the excitation from the $d_{x^2-y^2}$ to $d_{3z^2-r^2}$ orbitals, which is shifted to lower energy loss because of the increased cubic symmetry[34]. This is motivated by the relative intensity of the p1 peak to that of the main *dd*-excitations and by its behavior as a function of $Q_{\parallel}$ (see Supplementary Note 2).

RIXS calculations and ground state orbital symmetry inversion. Next we show, based on small-cluster exact diagonalization calculations, that a good agreement with the RIXS data can be obtained by assuming that the apical oxygen, O_{apex}, is closer to the interfacial Cu ion (than in the bulk) such that the Cu $d_{3z^2-r^2}$ orbital is strongly shifted up in energy, but remains slightly below the Cu $d_{x^2-y^2}$ level. The cluster is shown in Fig. 7a and consists of a CuO$_5$ pyramid linked to a MnO$_6$ octahedron through its apical oxygen ion. To account for the structural and electronic reconstruction, we allow the O_{apex} to have different electronic parameters than the in-plane oxygens (around the Cu ion). In particular, its energy is shifted closer to the reference Cu $d_{x^2-y^2}$ orbital and the Cu-O_{apex} hopping parameters $V_{pd\sigma}$, $V_{pd\pi}$ are larger than the in-plane Cu–O ones. The on-site Coulomb repulsion on the Cu and Mn ions is parametrized by the on-site Coulomb interaction between two *d* holes, U_{dd}.

The red curve in Fig. 7b shows a calculated RIXS spectrum (with π-polarized light and for the same geometry as in the experiment) at the Cu L$_3$-edge for a tetragonal crystal field environment of the Cu ion and a value of the Cu–O_{apex} hopping parameter that is twice the in-plane one. The enhanced hopping to O_{apex} pushes the crystal field towards a more cubic symmetry, in comparison to bulk YBCO[35]. This parameter configuration reproduces the main features of the

measured RIXS spectrum at the interface resonance. It yields a spectrum with narrow *dd*-excitations at about $\Delta E = -1.5$ eV and a small peak at $\Delta E = -0.6$ eV similar to the experimental one (see Figs. 4c and 5). Our cluster calculation further confirms that the p1 peak originates from exciting a hole into the Cu $d_{3z^2-r^2}$ orbital. Here, we used a standard value for the Coulomb interaction on the Mn site with $U_{dd} = 7.0$ eV, which is obtained by the Racah parameterization $U_{dd} = A + 4B + 3C$ given in ref. [36].

Now we explore the eventual effect of the Mn–COO on the RIXS spectra. The strength of the Mn on-site Coulomb interaction U_{dd} is expected to be modified by the Mn–COO, since it is renormalized in a solid (compared to the free ion case) due to screening effects of the environment. To assess for the influence of a local variation of U_{dd} at the Mn site on the orbital occupation of the Cu site, we vary U_{dd} and plot the hole occupation of the $d_{3z^2-r^2}$ and $d_{x^2-y^2}$ orbitals in Fig. 7c. There is a clear transition around $U_{dd}^c = 6.4$ eV, below which the main unoccupied orbital changes from $d_{x^2-y^2}$ to $d_{3z^2-r^2}$ (meaning that the $d_{3z^2-r^2}$ level of the interfacial Cu ions is located slightly above the $d_{x^2-y^2}$ level). Notably, this transition has a drastic effect on the Cu L$_3$-edge RIXS spectra, which essentially become silent in π-polarization, since the intensity of the RIXS spectra for $U_{dd} < U_{dd}^c = 6.4$ eV is negligibly small. This is shown by the blue curve in Fig. 7b for the same hopping parameters and *d*-orbital energies as before, but for $U_{dd} = 6.0$ eV. This dramatic reduction of the RIXS intensity for smaller values of U_{dd} can be explained by the combination of two effects. First, the hole occupation of the highest lying Cu orbital is reduced from 0.84 to 0.38 when U_{dd} is decreased, resulting in a strong loss of absorption in the first step of the RIXS process. Second, the change of symmetry of this orbital from $d_{x^2-y^2}$ to $d_{3z^2-r^2}$ leads to a global RIXS intensity diminution for π-polarized light as used here. With this result, we see that a small variation of U_{dd} has an enormous influence on the Cu L$_3$-edge RIXS spectrum.

Cu orbital order reconciles RIXS and XLD. At a first glance, the RIXS spectra seem to suggest that the $d_{3z^2-r^2}$ level of the interfacial Cu ions is located slightly below the $d_{x^2-y^2}$ level. However, the XLD data in Fig. 6c are not compatible with such a scenario for which the majority of the Cu related holes would reside on the $d_{x^2-y^2}$ level. The TEY signal in Fig. 6c, which is governed by the peaks I and II due to the interfacial Cu-ions, exhibits instead only a very small XLD signal, indicating that the holes are almost equally distributed between the $d_{3z^2-r^2}$ and $d_{x^2-y^2}$ levels. A natural way to reconcile the RIXS and XLD data is in terms of an alternation of the partially unoccupied Cu $d_{3z^2-r^2}$ and $d_{x^2-y^2}$ orbitals along the interface, as shown schematically in Fig. 7d. This alternation is stemming from a two-fold modulation by the Mn–COO of the onsite Mn Coulomb interaction U_{dd}, such that one Mn site out of two has U_{dd} below the critical value U_{dd}^c. As a consequence, across the NCSMO/YBCO interface, only one interfacial Cu site over two contributes to the Cu L$_3$-edge RIXS signal with a reconstructed spectrum as shown in Fig. 7b (red curve) indicating that a quasi-cubic coordination of the CuO$_5$ pyramids takes place. Our cluster simulation indicates that this alternation of Cu *d*-orbital occupation also leads to an alternation of the Mn *d*-orbital occupation on the other side of the interface, which is in line with the Mn–COO state (see Fig. 7d and Supplementary Note 3 for more details). This constitutes our second important finding: the Mn–COO order affects the orbital reconstruction of the interfacial Cu ions and likely causes a spatial modulation along the interface. Figure 5 confirms that a clear peak at -0.7 eV, due to the interfacial dd-excitation from $d_{x^2-y^2}$ to $d_{3z^2-r^2}$, occurs only in the presence of the Mn–COO, which yields a more homogenous electronic environment with two well-defined Mn sites. Without the Mn–COO, e.g., for the YBCO/LCMO SL,
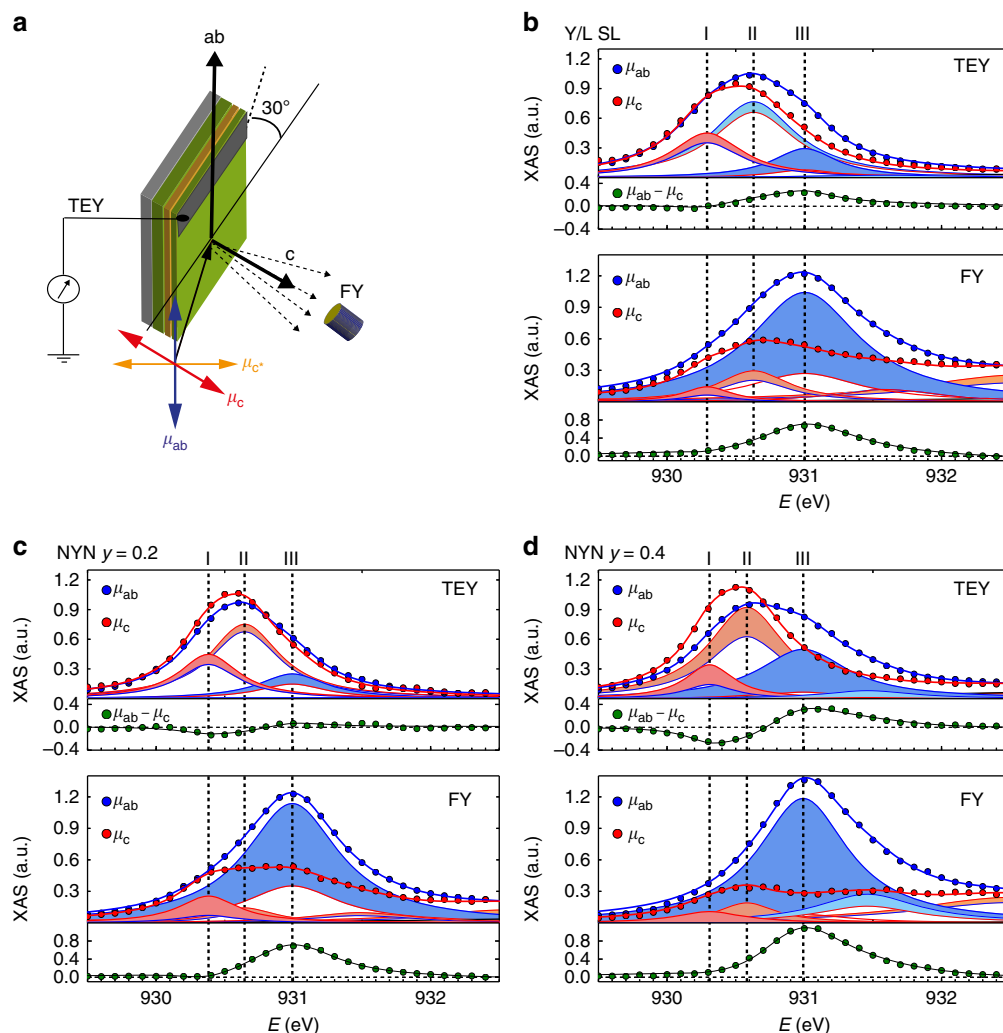
Fig. 6 X-ray linear dichroism (XLD) curves showing the orbital reconstruction of the interfacial Cu ions. **a** Schematic view of the x-ray linear dichroism experiment in total electron yield (TEY) and fluorescence yield (FY) mode. The linear polarization of the incident x-rays (at 30 degree with respect to film surface) is indicated by the red and blue arrows for the in-plane and the out-of-plane components, respectively. **b–d** Comparison of the XAS spectra of the NYN trilayers with $y = 0.2$ and $y = 0.4$ and a YBa$_2$Cu$_3$O$_7$/La$_{2/3}$Ca$_{1/3}$MnO$_3$ (YBCO/LCMO) superlattice. Shown are the Cu L_3 -edge spectra taken at $T = 5$ K and $H = 0.5$ T in TEY mode (top panel), which predominantly probes the top-most YBCO/manganite interface, and in FY mode (bottom panel) which is sensitive to all Cu ions. The experimental data are shown by solid symbols, the peak fitting with four Lorentzian functions as lines. The peaks (I) and (II) at 930.4 eV and 930.6 eV (that are strongest in TEY mode) are attributed to interfacial Cu ions whereas the peak (III) at 931 eV arises from the bulk-like Cu ions (that are much stronger in FY mode). The sign of the dichroism of the individual peaks is indicated by the shading

there is still a pronounced narrowing and red-shift of the *dd*-excitations around −1.5 eV, signaling that the same kind of orbital reconstruction occurs as in the NYN trilayers, but the p1 peak is strongly broadened and thus barely visible. This broadening most likely reflects the more disordered Mn environment at the YBCO/ LCMO interface with a so-called "dead layer"[18,20,22] at which the FM order is strongly suppressed and the charge carriers accordingly are localized but more randomly distributed than in the presence of the Mn–COO.

Discussion
The coupling mechanism between the Mn–COO, the orbital reconstruction of the interfacial Cu ions and the Cu-CDW order of the bulk-like Cu ions remains to be understood. The direct coupling between the Mn–COO (with a twofold period of the charge order along the Mn-O bond direction and a fourfold

period of the orbital ordering along the diagonal)[9,10] and the Cu-CDW (with an incommensurate, nearly three-fold period along the Cu–O bonds) should be rather weak. Nevertheless, the static Cu-CDW can be stabilized (pinned) by the domain boundaries of the Mn–COO or by the lattice distortions that accompany the Mn–COO[9,10]. An anomalously strong coupling between the phonon modes of the cuprate and manganite layers was indeed reported for YBCO/LCMO superlattices[37].

In summary, we have uncovered that the magnitude of the Cu-CDW in NYN trilayers is determined by the strength of the Mn–COO. Since the latter can be readily controlled via the tolerance factor or even by the application of a magnetic field or intense photon beams or pulses[9,37,38], these multilayers emerge as a unique platform for studying the relationship between the Cu-CDW and superconductivity. New combined or intertwined charge/orbital ordered and superconducting quantum states may also be realized,
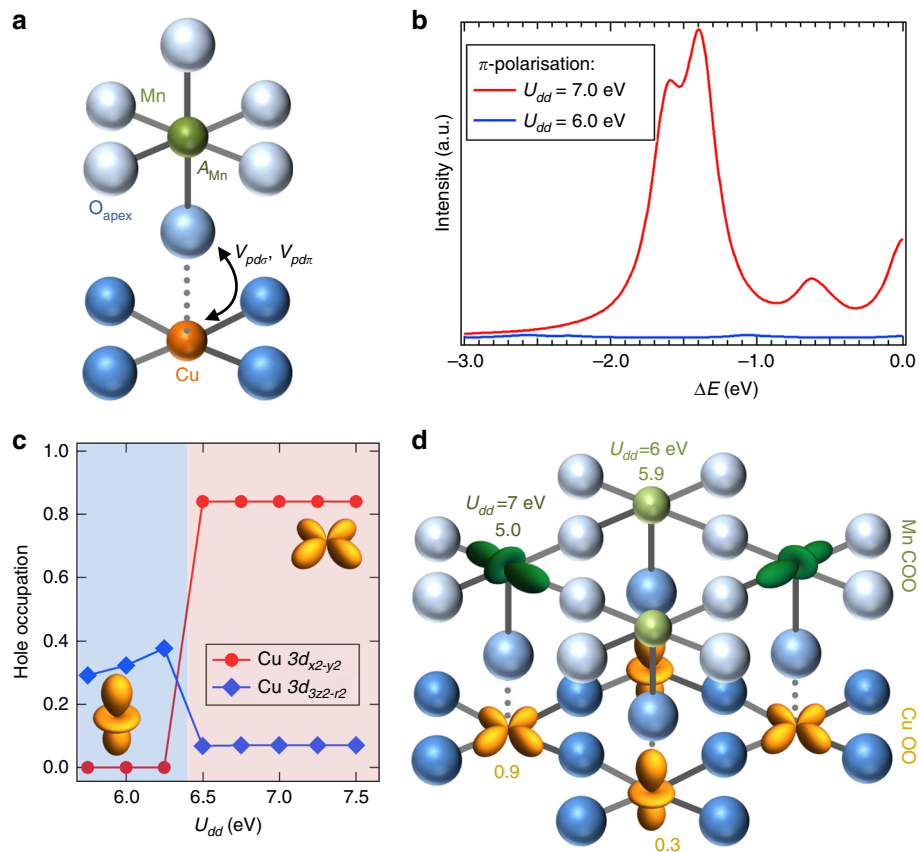
Fig. 7 Cluster calculations of the RIXS signal due to the *dd*-transitions of the interfacial Cu ions. **a** Schematic of the cluster containing the interfacial Cu and Mn ions that was used to calculate the RIXS spectra. **b** Calculated RIXS spectra with the *dd*-excitations at the Cu L_3-edge for two representative values of the Coulomb interaction on the Mn site U_{dd} at which the holes of the Cu ion reside primarily on the d_{x2-y2} (red line) and the d_{3z2-r2} levels (blue line), respectively. **c** Calculated values of the hole occupation of the d_{x2-y2} and d_{3z2-r2} orbitals as a function of U_{dd} which indicate a sudden change at around $U_{dd} = $ 6.4 eV. **d** Sketch of the orbital order at the NCSMO/YBCO interface showing the alternation of the partially unoccupied Cu $3d$ orbitals (orange) which follows the Mn–COO (light and dark green symbols). The colored numbers indicate the average hole occupation for the Cu and Mn d states

e.g., by increasing the hole doping, x, of the manganite, which leads to different domain states and ordering types of the Mn–COO[9,10].

Methods

Sample growth and characterization. Trilayers of $Nd_{0.65}(Ca_{1-y}Sr_y)_{0.35}MnO_3(26$ nm)/$YBa_2Cu_3O_7(7$ nm)/$Nd_{0.65}(Ca_{1-y}Sr_y)_{0.35}MnO_3(13$ nm) with $y = 0.2$ and 0.4 and a 1 nm thick $LaAlO_3$ capping layer were grown on (001)-oriented $La_{0.3}Sr_{0.7}Al_{0.65}Ta_{0.35}O_3$ (LSAT) substrates with pulsed laser deposition (PLD) using an excimer KrF laser ($\lambda = 248$ nm, $t_s = 25$ ns). Details about the growth conditions and the sample characterization can be found in the Supplementary Notes 4 and 5.

Resonant inelastic X-ray scattering (RIXS). The RIXS experiments at the Cu L_3-edge have been performed at the ADRESS beamline[39,40] of the Swiss light source (SLS) at the Paul Scherrer Institute (PSI) in Switzerland. The energy resolution with a full width at half-maximum of 134 meV was determined by measuring the elastic scattering from a carbon-filled acrylic tape. We also measured the X-ray absorption in total electron yield (TEY) to calibrate the energy scale with respect to the one of the X-ray absorption spectroscopy data taken at the XTreme beamline. Accordingly, the energy scale of the incident energies used for the RIXS data has been shifted by -0.23 eV. A scattering angle (between the incoming and outgoing X-ray beams) of 130° was used.

XAS. The XLD experiments at the Cu L_3-edge have been performed in total electron yield (TEY) and fluorescence yield (FY) mode at the XTreme beamline[41] of the SLS at the Paul Scherrer Institute (PSI) in Switzerland. As shown in Fig. 6a, the angle of incidence of the X-ray beam was set to 30° such that the response in vertical polarization, μ_{VL}, corresponds to the *ab* plane response of YBCO, $\mu_{ab} = \mu_{VL}$, whereas the *c*-axis response, μ_c, is obtained from the signal in horizontal polarization (HL), $\mu_{HL} = \mu_{c^*}$ according to the geometrical factor,

$\mu_c = 1/(\cos^2(\theta)\mu_{HL} - \tan^2(\theta)\mu_{VL})$. The data in Fig. 6b–d have been normalized to the maximum of the polarization-averaged absorption $\mu_{avg} = \max[(2\mu_{ab} + \mu_c)/3]$ at the Cu L_3 edge.

Transport measurements. Resistance versus temperature measurements of NCSMO single layers with $y = 0.2$ and 0.4 were performed with a Quantum Design PPMS 9 T system using the 4-point probe technique. Copper wires were glued onto the corners of the samples using silver paste and a fixed DC current of $I = 10$ μA was applied and the voltage was measured with a Keithley 2602 digital multimeter 223 using a ramping rate of 2 K min^{-1}.

Raman spectroscopy. The Raman experiments were performed with a Jobin-Yvon LabRam HR800 spectrometer using the 632.8 nm excitation line of a HeNe laser. The measurements were carried out in full back scattering with geometry z(Y'X')z in Porto's notation. The laser was focused with a ×100 objective, which was positioned with an accuracy of < 0.5 μm, such that the focus was in the film[42]. Based on a reference measurement with a beam focus in the substrate, the substrate contribution was subtracted from the data. Laser heating effects were minimized by keeping the laser power < 1 mW, and the temperatures quoted have an uncertainty of at most 5 K[41].

X-ray diffraction (XRD). The X-ray diffraction measurements of two NYN trilayers with $y = 0.2$ and 0.4 have been performed with a four-circle diffractometer (Rigaku SmartLab) with a 9 kW rotating Cu-$K\alpha_1$ anode and an incident parallel beam optics that consist of a reflecting mirror and a two-bounce Ge (220) monochromator ($\Delta\lambda/\lambda = 3.8 \times 10^{-4}$). The instrument is equipped with a He-flow cryostat with a Beryllium dome for measurements between 4 and 300 K.

Cluster calculations. The RIXS intensity was evaluated using the Kramers-Heisenberg formalism[31], where the initial, intermediate, and final states of the RIXS process were obtained from small cluster exact diagonalization calculations on a small (CuO_5) (MnO_6) cluster, as shown in Fig. 7a. The cluster included all five of the Cu and Mn $3d$ orbitals, as well as the O $2p$ orbitals oriented along each of the TM-O bonds (twenty orbitals in total). The model included the full rotationally-symmetric Hubbard and Hund inter-orbital and intra-orbital interactions on both the Mn and Cu $3d$ orbitals (within the Racah parameterization), the onsite Hubbard interaction on the O sites, and the nearest neighbor hopping given by the Slater-Koster parameterization. The cluster Hamiltonian was diagonalized in the ($N_\uparrow = 5$, $N_\downarrow = 2$) hole sector, using open boundary conditions. Full details of the model are given in the Supplementary Note 3.

References

1. Keimer, B., Kivelson, S. A., Norman, M. R., Uchida, S. & Zaanen, J. From quantum matter to high-temperature superconductivity in copper oxides. *Nature* **518**, 179 (2015).
2. Wu, T. et al. Magnetic-field-induced charge-stripe order in the high-temperature superconductor $YBa_2Cu_3O_y$. *Nature* **477**, 191–194 (2011).
3. Ghiringhelli, G. et al. Long-Range Incommensurate Charge Fluctuations in (Y, Nd)$Ba_2Cu_3O_{6+x}$. *Science* **337**, 821 (2012).
4. Chang, J. et al. Direct observation of competition between superconductivity and charge density wave order in $YBa_2Cu_3O_{6.67}$. *Nat. Phys.* **8**, 871–876 (2012).
5. Wu, T. et al. Incipient charge order observed by NMR in the normal state of $YBa_2Cu_3O_y$. *Nat. Commun.* **6**, 6438 (2015).
6. Chang, J. et al. Magnetic field controlled charge density wave coupling in underdoped $YBa_2Cu_3O_{6+x}$. *Nat. Commun.* **7**, 11494 (2016).
7. Gerber, S. et al. Three-dimensional charge density wave order in $YBa_2Cu_3O_{6.67}$ at high magnetic fields. *Science* **350**, 949 (2015).
8. Fradkin, E., Kivelson, S. A. & Tranquada, J. M. Theory of intertwined orders in high temperature superconductors. *Rev. Mod. Phys.* **87**, 457–482 (2015).
9. Tokura, Y. Critical features of colossal magnetoresistive manganites. *Rep. Prog. Phys.* **69**, 797–851 (2006).
10. Tokura, Y. & Tomioka, Y. Colossal magnetoresistive manganites. *J. Magn. Magn. Mater.* **200**, 1–23 (1999).
11. Millis, A. J., Littlewood, P. B. & Shraiman, B. I. Double exchange alone does not explain the resistivity of $La_{1-x}Sr_xMnO_3$. *Phys. Rev. Lett.* **74**, 5144–5147 (1995).
12. Efremov, D. V., van den Brink, J. & Khomskii, D. I. Bond- versus site-centred ordering and possible ferroelectricity in manganites. *Nat. Mater.* **3**, 853–856 (2004).
13. Ferrari, V., Towler, M. & Littlewood, P. B. Oxygen Stripes in $La_{0.5}Ca_{0.5}MnO_3$ from Ab Initio Calculations. *Phys. Rev. Lett.* **91**, 227202 (2003).
14. Jooss, C. et al. Polaron melting and ordering 331 as key mechanisms for colossal resistance effects in manganites. *Proc. Natl. Acad. Sci. U. S. A* **104**, 13597–13602 (2007).
15. Wu, L., Klie, R. F., Zhu, Y. & Jooss, C. Experimental confirmation of Zener-polaron-type charge and orbital ordering in $Pr_{1-x}Ca_xMnO_3$. *Phys. Rev. B* **76**, 174210 (2007).
16. Chakhalian, J. et al. Orbital Reconstruction and Covalent Bonding at an Oxide Interface. *Science* **318**, 1114 (2007).
17. Chakhalian, J. et al. Magnetism at the interface between ferromagnetic and superconducting oxides. *Nat. Phys.* **2**, 244–248 (2006).
18. Hoffmann, A. et al. Suppressed magnetization in $La_{0.7}Ca_{0.3}MnO_3/YBa_2Cu_3O_{7-\delta}$ superlattices. *Phys. Rev. B* **72**, 140407 (2005).
19. Peña, V. et al. Giant Magnetoresistance in Ferromagnet/Superconductor Superlattices. *Phys. Rev. Lett.* **94**, 057002 (2005).
20. Satapathy, D. K. et al. Magnetic Proximity Effect in $YBa_2Cu_3O_7/La_{2/3}Ca_{1/3}MnO_3$ and $YBa_2Cu_3O_7/LaMnO_{3+\delta}$ Superlattices. *Phys. Rev. Lett.* **108**, 197201 (2012).
21. Sefrioui, Z. et al. Ferromagnetic/superconducting proximity effect in $La_{0.7}Ca_{0.3}MnO_3/YBa_2Cu_3O_{7-\delta}$ superlattices. *Phys. Rev. B* **67**, 214511 (2003).
22. Stahn, J. et al. Magnetic proximity effect in perovskite superconductor/ferromagnet multilayers. *Phys. Rev. B* **71**, 140509 (2005).
23. Visani, C. et al. Equal-spin Andreev reflection and long-range coherent transport in high temperature superconductor/half-metallic ferromagnet junctions. *Nat. Phys.* **8**, 539–543 (2012).
24. Salafranca, J. et al. Competition between Covalent Bonding and Charge Transfer at Complex-Oxide Interfaces. *Phys. Rev. Lett.* **112**, 196802 (2014).
25. Varela, M., Lupini, A. R., Pennycook, S. J., Sefrioui, Z. & Santamaria, J. Nanoscale analysis of $YBa_2Cu_3O_{7-x}/La_{0.67}Ca_{0.33}MnO_3$ interfaces. *Solid State Electron.* **47**, 2245–2248 (2003).
26. Mallett, B. P. P. et al. Granular superconductivity and magnetic-field-driven recovery of macroscopic coherence in a cuprate/manganite multilayer. *Phys. Rev. B* **94**, 180503(R) (2016).
27. Frano, A. et al. Long-range charge-density-wave proximity effect at cuprate/manganate interfaces. *Nat. Mater.* **15**, 831–834 (2016).
28. He, J. et al. Observation of a three-dimensional quasi-long-range electronic supermodulation in $YBa_2Cu_3O_{7-x}/La_{0.7}Ca_{0.3}MnO_3$ heterostructures. *Nat. Commun.* **7**, 10852 (2016).
29. Ament, L. J. P., van Veenendaal, M., Devereaux, T. P., Hill, J. P. & van den Brink, J. Resonant inelastic x-ray scattering studies of elementary excitations. *Rev. Mod. Phys.* **83**, 705–767 (2011).
30. Blanco-Canosa, S. et al. Resonant x-ray scattering study of charge-density wave correlations in $YBa_2Cu_3O_{6+x}$. *Phys. Rev. B* **90**, 054513 (2014).
31. Achkar, A. J. et al. Distinct charge orders in the planes and chains of ortho-III-ordered $YBa_2Cu_3O_{6+\delta}$ superconductors identified by resonant elastic X-ray scattering. *Phys. Rev. Lett.* **109**, 167001 (2012).
32. Dediu, V. et al. Jahn-Teller dynamics in charge-ordered manganites from Raman spectroscopy. *Phys. Rev. Lett.* **84**, 4489 (2000).
33. Sen, K. et al. X-ray absorption study of the ferromagnetic Cu moment at the $YBa_2Cu_3O_7/La_{2/3}Ca_{1/3}MnO_3$ interface and variation of its exchange interaction with the Mn moment. *Phys. Rev. B* **93**, 205131 (2016).
34. Moretti Sala, M. et al. Energy and symmetry of dd excitations in undoped layered cuprates measured by Cu L_3 resonant inelastic x-ray scattering. *New J. Phys.* **13**, 043026 (2011).
35. Magnuson, M. et al. Self-doping processes between planes and chains in the metal-to superconductor transition of $YBa_2Cu_3O_{6.9}$. *Sci. Rep.* **4**, 7017 (2014).
36. Ishihara, S., Hatakeyama, T. & Maekawa, S. Magnetic ordering, orbital ordering, and resonant x-ray scattering in perovskite titanates. *Phys. Rev. B* **65**, 064442 (2002).
37. Kiryukhin, V. et al. An X-ray-induced insulator-metal transition in a magnetoresistive manganite. *Nature* **386**, 813–815 (1997).
38. Beaud, P. et al. A time-dependent order parameter for ultrafast photoinduced phase transitions. *Nat. Mater.* **13**, 923–927 (2014).
39. Ghiringhelli, G. et al. SAXES, a high resolution spectrometer for resonant x-ray emission in the 400–1600 eV energy range. *Rev. Sci. Instrum.* **77**, 113108 (2006).
40. Strocov, V. N. et al. High-resolution soft X-ray beamline ADRESS at the Swiss light source for resonant inelastic X-ray scattering and angle-resolved photoelectron spectroscopies. *J. Synchrotron Rad.* **17**, 631–643 (2010).
41. Piamonteze, C. et al. X-Treme beamline at SLS: X-ray magnetic circular and linear dichroism at high field and low temperature. *J. Synchrotron Rad.* **19**, 661–674 (2012).
42. Hepting, M. et al. Tunable charge and spin order in $PrNiO_3$ thin films and superlattices. *Phys. Rev. Lett.* **113**, 227206 (2014).

Author contributions
J.K. and E.P. grew and characterized the samples. The RIXS experiment was done by E.P., C.M., C.B., M.D., J.P., and T.S., the XAS by E.P., J.K., R.G., C.B., and C.P., the Raman by